Localizing the non-thermal X-ray emission of PSR J2229+6114 from its multi-wavelength pulse profiles

Jérôme Pétri, Sebastien Guillot, Lucas Guillemot, Dipanjan Mitra, Matthew Kerr, Lucien Kuiper, Ismaël Cognard, Gilles Theureau

A&A, 687, L13 (2024)
https://doi.org/10.1051/0004-6361/202450538

Astronomy & Astrophysics

LETTER TO THE EDITOR

Localizing the non-thermal X-ray emission of PSR J2229+6114 from its multi-wavelength pulse profiles

Jérôme Pétri[1], Sebastien Guillot[2], Lucas Guillemot[3,4], Dipanjan Mitra[5,6], Matthew Kerr[7], Lucien Kuiper[8], Ismaël Cognard[3,4], and Gilles Theureau[3,4,9]

[1] Université de Strasbourg, CNRS, Observatoire astronomique de Strasbourg, UMR 7550, 67000 Strasbourg, France
e-mail: jerome.petri@astro.unistra.fr
[2] IRAP, CNRS, 9 avenue du Colonel Roche, BP 44346, 31028 Toulouse Cedex 4, France
[3] Laboratoire de Physique et Chimie de l'Environnement et de l'Espace, Université d'Orléans/CNRS, 45071 Orléans Cedex 02, France
[4] Observatoire Radioastronomique de Nançay, Observatoire de Paris, Université PSL, Université d'Orléans, CNRS, 18330 Nançay, France
[5] National Centre for Radio Astrophysics, Tata Institute for Fundamental Research, Post Bag 3, Ganeshkhind, Pune 411007, India
[6] Janusz Gil Institute of Astronomy, University of Zielona Góra, ul. Szafrana 2, 65-516 Zielona Góra, Poland
[7] Space Science Division, Naval Research Laboratory, Washington, DC 20375-5352, USA
[8] SRON-Netherlands Institute for Space Research, Niels Bohrweg 4, 2333, CA Leiden, The Netherlands
[9] LUTH, Observatoire de Paris, Université PSL, Université Paris Cité, CNRS, 92195 Meudon, France

Received 29 April 2024 / Accepted 31 May 2024

ABSTRACT

Context. Pulsars are detected over the whole electromagnetic spectrum, from radio wavelengths up to very high energies, in the GeV-TeV range. While the radio emission site for young pulsars is well constrained to occur at altitudes about several percent of the light-cylinder radius and γ-ray emission is believed to be produced in the striped wind, outside the light cylinder, the non-thermal X-ray production site remains unknown.
Aims. The aim of this Letter is to localize the non-thermal X-ray emission region based on a multi-wavelength pulse profile fitting for PSR J2229+6114, which stands as a particularly good candidate given its high X-ray brightness.
Methods. Based on the geometry deduced from the joint radio and γ-ray pulse profiles, we fixed the magnetic axis inclination angle and the line-of-sight (LoS) inclination angle. However, we left the region of X-ray emission unlocalized, setting it somewhere between the surface and the light cylinder. We localized this region and its extension by fitting the X-ray pulse profile as observed by the NICER, *NuSTAR*, and RXTE telescopes in the ranges of 2–7 keV, 3–10 keV, and 9.4–22.4 keV, respectively.
Results. We constrained the non-thermal X-ray emission to arise from altitudes between $0.2\,r_{\rm L}$ and $0.55\,r_{\rm L}$ where $r_{\rm L}$ is the light-cylinder radius. The magnetic obliquity is approximately $\alpha \approx 45^\circ - 50^\circ$ and the LoS inclination angle is $\zeta \approx 32^\circ - 48^\circ$.
Conclusions. This Letter is among the first works to offer a tight constraint on the location of non-thermal X-ray emission from pulsars. We plan to apply this procedure to several other promising candidates to confirm this new result.

Key words. acceleration of particles – magnetic fields – radiation mechanisms: general – radiation mechanisms: non-thermal – stars: neutron – pulsars: individual: PSR J2229+6114

1. Introduction

Among the almost 3000 pulsars detected thus far, a substantial fraction of the γ-ray emitters are radio-loud. For the subclass of young pulsars, the radio phenomenology is well constrained and understood as coming from an emission cone located at a height about several hundred kilometres above the stellar surface, in the region where the dipole magnetic field is dominant (Mitra 2017). These results were obtained from the radio polarization data, interpreted using the rotating vector model (Radhakrishnan & Cooke 1969). The high brightness temperatures of the radio emission require a collective or coherent emission mechanism. Based on the emission region constraint, coherent curvature radiation (CCR) via charge bunches has been invoked as the plausible emission mechanism at work in this scenario. Moreover, several works have used either analytical methods, force-free electrodynamics (FFE) simulations, or particle-in-cell simulations to find a convergence to the same γ-ray emission site; namely the current sheet of the striped wind outside the light cylinder (e.g. Pétri 2011; Pétri & Mitra 2021; Cerutti et al. 2016). Two competing emission mechanisms are thought to produce these high-energy photons: incoherent curvature and synchrotron radiation. However, the non-thermal X-ray emission is not as well understood or studied as broadly. Thus, there is currently no concrete evidence to support its origin.

This Letter is aimed at constraining the location of the non-thermal X-ray emission, based on the geometry deduced from the combined radio and γ-ray pulse profile fitting. To apply this technique, good pulsar candidates should be seen in all three wavelength domains with a well-defined pulse profile in the non-thermal X-ray range (above 1–2 keV) to avoid contamination from the surface thermal X-ray emission. We found that

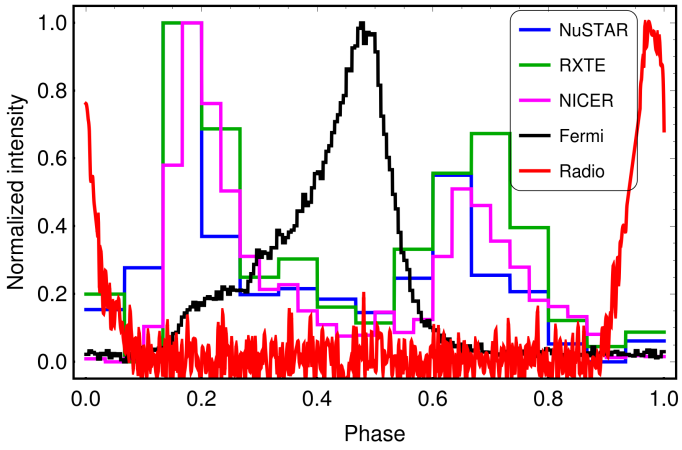

Fig. 1. Multi-wavelength light curves of PSR J2229+6114 as observed in radio with the Lovell telescope at the Jodrell Bank Observatory (1.5 GHz, red line), in X-ray with *NuSTAR* (3–10 keV, blue line), RXTE (9.4–22.4 keV, green line), NICER (2–6.9 keV, magenta line), and in γ rays with *Fermi* LAT (≥100 MeV, black line).

PSR J2229+6114 satisfies all the requirements for our purposes. This pulsar was discovered by Halpern et al. (2001) in radio and X-rays, pulsating at a period of $P \approx 51.6$ ms and with a spin-down rate of $\dot{P} \approx 7.83 \times 10^{-14}$ s/s. Its light-cylinder radius is about $r_{\rm L} = cP/2\pi = 2,462$ km where c is the speed of light. Its typical surface magnetic field is therefore estimated from the magneto-dipole losses (Pétri 2016) to be around 2×10^8 T and its strength at the light cylinder to 23 T assuming a dipole-like radial decrease, r^{-3}. This pulsar was later detected by the *Fermi* Large Area Telescope (LAT) instrument in the γ-ray energy range of [100 MeV,100 GeV] by Abdo et al. (2009). They reported a phase lag between the strongest XMM-Newton X-ray peak in the 1–10 keV range and the peak in radio of about 0.17 ± 0.02. Pétri (2011) previously fit the γ-ray pulse profile of PSR J2229+6114 with a split monopole solution, whereas more recently, Pétri & Mitra (2021) used a full 3D force-free magnetosphere model with a dipole field close to the surface. They found a magnetic obliquity of $\alpha \approx 35°$ and a line-of-sight (LoS) inclination angle of $\zeta \approx 44°$. In this Letter, we use joint radio and γ-ray data as well as new simulations with an emission height for the radio beam fixed at $R/r_{\rm L} = 0.1$, as deduced from radio polarization observations and fitted with the rotating vector model, including the aberration and retardation effects (Johnston et al. 2023).

In Sect. 2, we present some details of the data sets used in this work. The radio and γ-ray fitting results are summarized in Sect. 3 and extended by simultaneously joining the non-thermal X-ray pulse profile. The underlying expected particle dynamics and its energetics are discussed in Sect. 4. Our conclusions are given in Sect. 5.

2. Multi-wavelength data sets

2.1. Radio and γ-ray pulse profiles

We started by investigating the radio and γ-ray pulse profiles using the *Fermi*-LAT instrument, a wide-field-of-view (FoV) γ-ray telescope operating in the energy band 20 MeV to 300 GeV. (Atwood et al. 2009). Fig. 1 summarizes the *Fermi*-LAT pulse profile for energies above 0.1 GeV (black histograms), obtained by analyzing LAT data recorded between August 2008 and January 2023. The gamma-ray photon arrival times were phase-folded using a timing solution for PSR J2229+6114, extracted from the same *Fermi* LAT dataset, using the techniques presented in Ajello et al. (2022). The *Fermi* LAT Third Catalog of Gamma-ray Pulsars (3PC; Smith et al. 2023) reported a double peaked γ-ray pulse profile, showing a peak separation of $\Delta = 0.222 \pm 0.001$ and a γ-ray time lag of $\delta = 0.296 \pm 0.001$ between γ and radio. The timing solution constructed for this work uses the same radio fiducial phase (see e.g., Smith et al. 2023, for details) as the timing solutions for this pulsar from the *Fermi* LAT Second Catalog of Gamma-ray Pulsars (2PC; Abdo et al. 2013) and from 3PC; thus, the radio and gamma-ray phase separation in Fig. 1 is consistent with that in the latter catalogs. The 1.4 GHz radio profile in this figure was taken from the 2PC auxiliary files archive, corresponding to a profile recorded with the Lovell telescope at the Jodrell Bank Observatory (UK).

2.2. X-ray band

We used several instruments in the X-ray band, namely, Neutron star Interior Composition ExploreR (NICER, Gendreau et al. 2012), *Rossi* X-ray Timing Explorer (RXTE, Rothschild et al. 1998), and *NuSTAR* (Nuclear Spectroscopic Telescope Array, Harrison et al. 2013). Altogether they provide sufficient coverage from the soft to the hard X-rays (1–60 keV). The pulse profiles have also been phase-aligned with the radio profile, a crucial prerequisite for our model.

2.2.1. NICER pulse profile

The NICER observations of PSR J2229+6114 from 2018-02-02 22:59:00 to 2022-12-29 06:55:40 (ObsID 1033370101–5033370272) were used to generate the X-ray pulse profile analyzed here. The data were re-processed with the standard recommended procedure, using `nicerl2` of `NICERDAS` v10 and calibration file v20221001, distributed with `HEASOFT v6.31`. Following this approach, we employed the `NICERsoft` package[1] to further filter the data, excluding periods with 1) Earth magnetic cut-off rigidity `COR_SAX` < 1.5 GeV/c; 2) space weather index KP ≥ 5; 3) overshoot rates larger than 1.5 c/s; and 4) undershoot rates larger than 600 c/s. We also removed observation periods with a 2–10 keV count rate >1 c/s (averaged over 32 s) to exclude any possible remaining periods with a high background.

After this careful filtering process, the event files of the remaining ObsIDs were merged and the phases of all detected events were calculated using `photonphase` (from `PINT`[2]). The phase-folding was carried out using the timing solution for PSR J2229+6114 extracted from *Fermi* LAT data, as mentioned in Sect. 2.1, whose validity interval encompasses the NICER dataset. The NICER pulse profile is presented in Figs. 1 (purple histogram) and 3 (top panel). It was obtained in the 1.05–6.9 keV energy interval (after optimization, following Guillot et al. 2019).

2.2.2. RXTE-PCA pulse profile

The hard X-ray profile (9.4–22.4 keV) used in this work (see Fig. 1, green histogram, and Fig. 3, bottom panel) was adopted from Kuiper & Hermsen (2015). These authors compiled RXTE-PCA profiles of PSR J2229+6114 for two different energy bands, 1.9–9.4 keV and 9.4–22.4 keV, from a combination of two observation runs, totaling an exposure time of 220.2 ks. More detailed information on the RXTE PCA analysis can be found in Sect. 5.18 of Kuiper & Hermsen (2015).

[1] https://github.com/paulray/NICERsoft
[2] https://github.com/nanograv/PINT

2.2.3. *NuSTAR* pulse profile

The hard X-ray telescope *NuSTAR* (Harrison et al. 2013), operating in the 3–79 keV range, observed PSR J2229+6114 and its pulsar wind nebula (the Boomerang) for about 45.2 ks between September 21–22, 2020 (MJD 59114.012-59114.99). We used the "default" screened event files and converted the event arrival times to Solar System Barycentre arrival times, adopting the Solar System ephemeris DE405 and *NuSTAR* clock correction file nuCclock20100101v137.fits, yielding time tags with an absolute timing accuracy of better than 100 µs (Bachetti et al. 2021) that are amply sufficient to study the timing signal of PSR J2229+6114. Next, events were selected from a circular extraction radius of 90″ centered on the pulsar. The radio-aligned pulse profile for events with measured energies in the 10–60 keV band (=RXTE PCA analogon) is shown in Fig. 1 (blue histogram). The Z_n^2 significance, specifying the deviation from uniformity, is about 8.3σ, adopting 8 harmonics ($n = 8$). For the spectral energy distribution in X-ray and γ-ray, we refer to examples in Fig. 28 of Kuiper & Hermsen (2015), Fig. 2 of Íñiguez Pascual et al. (2022), and Fig. 3 of Coti Zelati et al. (2020).

3. Multi-wavelength pulse profile fitting

Conducting a simultaneous investigation of the radio and γ-ray pulse profiles allowed us to constrain the most probable value of the magnetic obliquity and LoS inclination angle. Localizing the height of the X-ray emission site is another goal of this study. In this section, we show a self-consistent view of the pulsar geometry in agreement with the three pulse profiles. We proceeded by following a two-step procedure. In the first stage, we fit the γ-ray profile and its time lag with respect to the radio peak to extract the magnetic obliquity, α, and LoS inclination angle, ζ. In a second stage, we added the X-ray emission zone, allowing the emission to start above the radio emission site at $0.2\,r_{\rm L}$ nearly all the way to the light cylinder. This was done to deduce the extension and altitude of this new region.

3.1. Radio and γ-ray emission

PSR J2229+6114 was studied more than a decade ago by Pétri (2011), who found $\alpha = 45°$ and $\zeta = 40°$, assuming a simple split monopole current sheet geometry. More recently, Pétri & Mitra (2021) found $\alpha = 35°$ and $\zeta = 44°$ with an accurate dipole force-free magnetosphere numerical solution. Here, we have reanalyzed the latter model, from the latest force-free magnetosphere simulations (Pétri 2024) with $r/r_{\rm L} = 0.1$. The accuracy of the obliquity α will be within $\Delta\alpha = 5°$ as the simulations were performed with this angle increment, $\Delta\alpha$. Because we detected both radio and γ-ray photons, the condition $\alpha \approx \zeta$ must apply within an error bar related to the opening angle of the radio emission cone, $\delta_{\rm rc}$. From Pétri (2011), we know that $\cos(\pi\,\Delta) = |\cot\alpha\,\cot\zeta|$ and, thus, we have $\cos(\pi\,\Delta) = \cot^2\alpha$. Therefore, the obliquity is around $\alpha \approx \zeta \approx 48°$. Figure 2 shows the best fit by minimizing the residual, defined as:

$$\chi^2_\nu = \frac{1}{n-1}\sum_{i=1}^{n}\left(I_i^{\rm mod} - I_i^{\rm obs}\right)^2/\sigma_i^2. \quad (1)$$

Here, n is the number of data points, $\nu = n - 1$, $I_i^{\rm obs}$ is the observed γ-ray flux, and $I_i^{\rm mod}$ is the predicted γ-ray normalized intensity, while σ_i represents the uncertainties in the gamma-ray flux. As a best fit, we chose an inclination of the magnetic dipole of $\alpha = 45°$ and an observer LoS angle of $\zeta = 38°$. These angles are deduced by minimizing χ^2_{n-1} in Eq. (1). The fit is excellent for the strongest peak, but worse for the weak peak, which is more pronounced in the energy band of 50 MeV-300 MeV. Moreover, knowing the radio pulse profile width, W, we can estimate the radio emission cone half-opening angle $\delta_{\rm rc}$ from Gil et al. (1984):

$$\sin(\delta_{\rm rc}/2) = \sqrt{\sin^2(W/4)\,\sin\alpha\,\sin(\alpha+\beta) + \sin^2(\beta/2)}. \quad (2)$$

The observed width, W, assumes that the full cone is visible at each rotation. The LoS must then satisfy $|\alpha - \zeta| < \delta_{\rm rc}$ in order to cross the radio beam. With the fit described above, we get for PSR J2229+6114 an opening angle of $\delta_{\rm rc} \approx 25°$. Assuming a dipole field structure, the radio emission height becomes $h/r_{\rm L} \approx (4/9)\,\delta_{\rm rc}^2 \approx 0.084$; therefore, it is slightly less than 10% of the light cylinder. This is consistent with the emission height estimated from radio polarization measurements (Mitra 2017; Johnston et al. 2023).

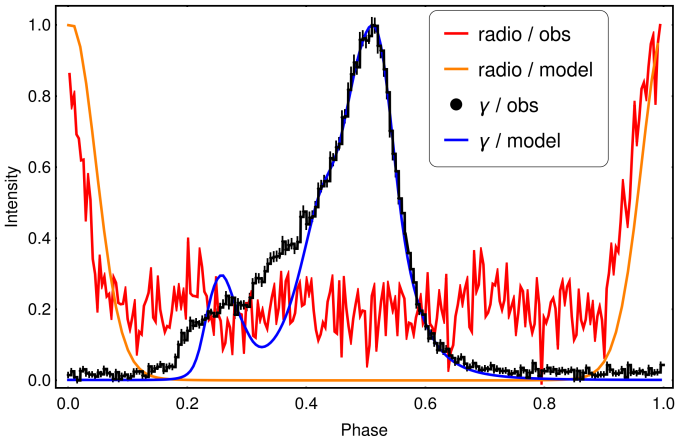

Fig. 2. Best fit for the phase-aligned γ-ray light-curve (≥100 MeV) of PSR J2229+6114 with $(\alpha, \zeta) = (45°, 38°)$. The radio pulse profile is shown in red, the model in orange, the γ-ray observations in black and our model in blue.

3.2. X-ray emission

To deduce the X-ray emission altitude and extension, we computed several atlases of pulse profiles, assuming that photons emanate from thin shells around the separatrix, namely, the surface representing the interface between closed and open magnetic field lines. We considered 15 shells with boundaries set along the magnetic field lines, an emissivity with a Gaussian profile in the direction perpendicular to the magnetic surface of width, $w_X = 0.1 r_{\rm L}$, and sharp cut offs at radii, r_1 and r_2, such that a shell is in the interval of $[r_1, r_2]$. These zones possess an extension in radius of $0.05\,r_{\rm L}$, cut in different spherical layers – from a first zone at a height of $r/r_{\rm L} \in [0.2, 0.25]$ to a last zone at a height of $r/r_{\rm L} \in [0.9, 0.95]$; therefore, the kth zone is $(r/r_{\rm L})_k \in [0.2 + 0.05\,k, 0.25 + 0.05\,k]$, starting from zone $k = 0$ to $k = 14$. From these atlases, we computed the pulse profiles by using only one zone or by adding several adjacent zones to determine the minimal and maximal emission heights compatible with the pulses. We also kept the LoS inclination angle, ζ, as a free parameter to check whether we were able to retrieve the same value as for the γ-ray light curve. For completeness, an obliquity with $\alpha = 50°$ and $\alpha = 40°$ was also tested. Performing the fits for NICER above 2 keV, for *NuSTAR* above 3 keV, and

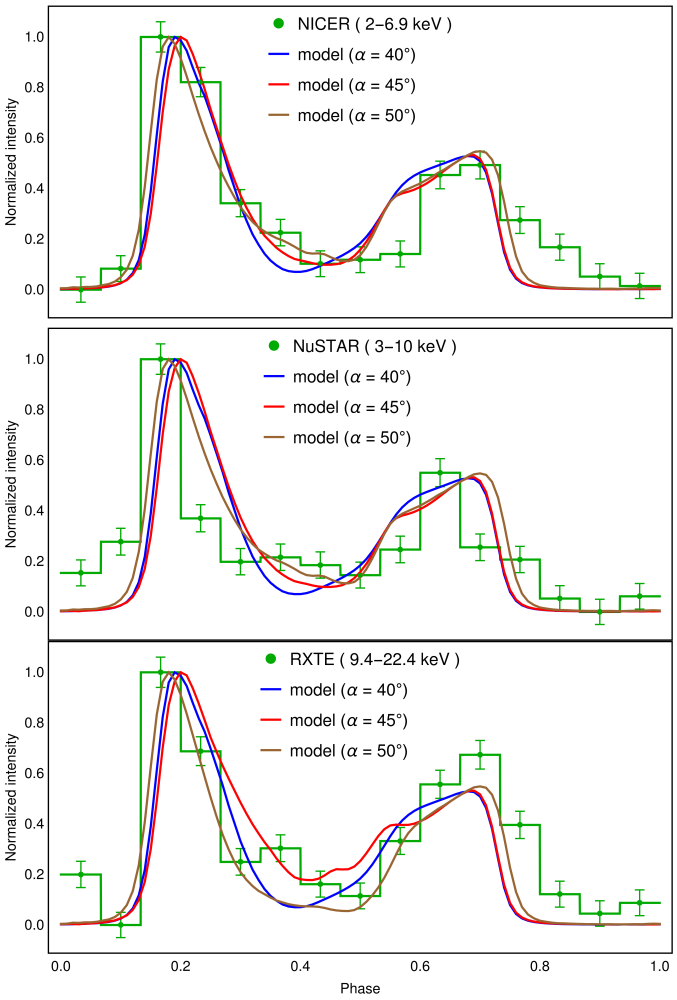

Fig. 3. Best-fit light-curves in X-rays, using the NICER data (top); *NuSTAR* data (middle); and RXTE data (bottom). Observations are shown in green and the models in blue for $(\alpha, \zeta) = (40°, 46°)$, in red for $(\alpha, \zeta) = (45°, 38°)$, and in brown for $(\alpha, \zeta) = (50°, 36°)$.

for RXTE in the band $[9.4, 22.4]$ keV, we get the results shown in Fig. 3. The top panel compares the NICER pulses in green to our model in blue for $\alpha = 40°$, in red for $\alpha = 45°$ and in brown for $\alpha = 50°$, giving a best fit of $\zeta = 46°$ for the blue curve, $\zeta = 38°$ for the red curve and $\zeta = 36°$ for the brown curve. The middle panel shows good fits for *NuSTAR* and the bottom panel for RXTE. In all cases, the emission starts at $r/r_{\rm L} = 0.2$ and goes up to an altitude of $r/r_{\rm L} = 0.55$ for all three panels in Fig. 3. Moreover, we used a consistent set of obliquities, α, and LoS inclination angle, ζ, for all light curves shown in Fig. 3 corresponding to the best fit for NICER observations. If the LoS is not constrained, the results are slightly different, depending on the instrument as summarized in Table 1. However, these values of ζ encompass the value found in the previous paragraph and are fully compatible.

We stress that our force-free model only provides the geometrical locations where the radiation is produced within the pulsar magnetosphere. The force-free simulations used in this work assume a star-centred dipole; hence, if the non-thermal X-rays originate from below the radio emission region, then the model predicts time aligned radio and non-thermal X-ray profiles, however, these are not consistent with the observations. Clearly, the expected width below the radio emission region is

Table 1. LoS inclination angles, ζ, implied by the non-thermal X-ray pulse profile obtained with NICER, RXTE, and *NuSTAR* data by imposing $\alpha = \{40°, 45°, 50°\}$.

Satellite	Band	$\alpha = 40°$	$\alpha = 45°$	$\alpha = 50°$
NICER	2–6.9 keV	46°	38°	36°
RXTE	9.4–22.4 keV	58°	48°	34°
NuSTAR	3–10 keV	58°	56°	50°

significantly smaller than the observed X-ray profile width. We also refer to Philippov et al. (2020), who suggested a different explanation related to the particles producing the radio emission. Realistically, the surface magnetic field is non-dipolar in nature (Pétri & Mitra 2020; Arumugasamy & Mitra 2019) and while this may explain the observed radio and non-thermal X-ray profile misalignment, it cannot explain the observed X-ray profile width – since the presence of a non-dipolar field will shrink the polar cap further resulting in a smaller pulse width, compared to the dipolar case. The fact that the non-thermal X-ray emission originates higher up in the magnetosphere is therefore a robust result.

4. Discussion on the energetics

In our force-free model, the region along the separatrix is the location where the non-thermal X-rays are generated. The charges that accelerate along the separatrix give rise to non-thermal X-ray emission by two possible mechanisms, namely, synchrotron or curvature radiation. The former requires a large pitch angle $\psi \sim 90°$ for the particles to significantly experience the magnetic gyro-motion. The latter requires motion along magnetic field lines with a possible perpendicular drift. This means a small pitch angle of $\psi \ll 1$ is required. For intermediate pitch angles, neither synchrotron nor curvature spectra applies, but synchro-curvature sets in instead. This synchro-curvature radiation has been studied in the context of pulsar magnetospheres by Kelner et al. (2015), where particles are forced to glide along the separatrix.

We go on to compute the expected particle characteristics in the force-free approximation. The magnetic field strength of the dipole is known from its spin-down and the field line curvature from the force-free model. Assuming a dipolar decrease of the magnetic field strength from the surface to the base of the wind, its strength at the light cylinder is about $B_{\rm L} \approx 23\ T$. In order to produce the required X-ray photons of energy $E_{\rm X}$, typically above 1 keV, the particle Lorentz factor must follow these values, in the curvature $\gamma_{\rm curv}$ and synchrotron $\gamma_{\rm sync}$ cases, respectively:

$$\gamma_{\rm curv} \approx 3.5 \times 10^5\ (E_{\rm X}/5\ {\rm keV})^{1/3}\ (\rho_{\rm c}/r_{\rm L})^{1/3}\,, \tag{3a}$$

$$\gamma_{\rm sync} \approx 1358\ (E_{\rm X}/5\ {\rm keV})^{1/2}\ (B/B_{\rm L})^{-1/2}\,, \tag{3b}$$

where $\rho_{\rm c}$ is the curvature radius of the particle trajectory, $B_{\rm L}$ is the magnetic field strength at the light cylinder, B is the magnetic field strength at the emission location. However, synchrotron radiation is very unlikely close to the stellar surface because particles stay in their fundamental Landau level. At larger distances, close to the light cylinder, this pitch angle could be measured from the radiation reaction limit velocity, as explained by Kalapotharakos (2019).

Moreover, from a theoretical point of view, in the pair cascade region above the polar cap, current models predict two populations of pair plasma flows: a primary beam (b) of electrons

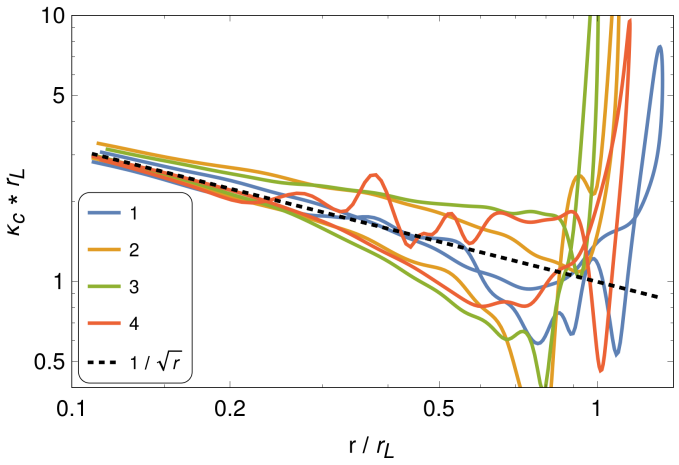

Fig. 4. Curvature in units of $1/r_{\rm L}$ along the separatrix starting from the surface going to the light cylinder and back to the surface for the force-free solution. Values are given for an oblique rotator with $\alpha = 45°$. At low heights, it follows $\kappa_{\rm c}\, r_{\rm L} \approx r^{-1/2}$. The four field lines are shown in different colours.

and positrons, with a very high Lorentz factor accelerated in the vacuum gap potential drop to reach $\gamma_{\rm b} \approx 10^6$ and a secondary plasma of $e^{\pm}$ pairs (p) produced by cascades due to magnetic photo-disintegration reaching Lorentz factors of $\gamma_{\rm p} \approx 10^2$ (Kazbegi et al. 1991; Arendt & Eilek 2002; Usov 2002). In the partially screened gap model of Gil et al. (2003), an ion outflow is allowed with $\gamma_{\rm ion} \approx 10^3$. Electrons and positrons do not follow exactly the same distribution functions because of the parallel electric field screening (Beskin et al. 1993). The pair multiplicity factor can reach values up to $\kappa \approx 10^4$–10^5 (Timokhin & Harding 2019). This pair plasma produces the observed radio emission, typically, in the MHz–GHz band, through CCR (Mitra 2017). The evolution of the curvature, $\kappa_{\rm c}$, along the particle path within the separatrix surface in a force-free magnetosphere plays a central role. It is shown in Fig. 4 for an obliquity of $\alpha = 45°$, in units of $1/r_{\rm L}$. Each colour depicts a different field line, with a sample of four representative lines having been chosen. The curvature decreases with distance to the star approximately like $r^{-1/2}$ for the FFE model (actually, it is the same behaviour for the vacuum case), as long as $r \ll r_{\rm L}$. Moreover at the radio emission height of $r/r_{\rm L} \approx 0.1$, this curvature is about $\kappa_{\rm c}\, r_{\rm L} = r_{\rm L}/\rho_{\rm c} \approx 22$–$35$. Therefore, the particle Lorentz factor for producing radio photons in the GHz band is $\gamma_{\rm radio} \approx 57\ (\nu_{\rm radio}/1\,{\rm GHz})^{1/3}\ (30\,\rho_{\rm c}/r_{\rm L})^{1/3}$. This corresponds to the secondary plasma flow with $\gamma_{\rm radio} \approx 100$ for typical values of $\rho_{\rm c}$. If the X-ray photons are produced in regions with a similar curvature, then the Lorentz factor ratio must be $\gamma_{\rm X}/\gamma_{\rm radio} = (5\,{\rm keV}/h \times 1\,{\rm GHz})^{1/3} \approx 10^3$. This corresponds to the primary beam with Lorentz factor of about 10^{4-5}, which is consistent with the estimates for primary beams, as, for instance, reported by Timokhin & Arons (2013). However, the core of the X-ray emission approaches $r \approx 0.5\, r_{\rm L}$ where the curvature has decreased by a factor of 2–3, down to $\kappa_{\rm c}\, r_{\rm L} \approx 10$, requiring $\gamma_{\rm X} \approx 1.6 \times 10^5\ (E_{\rm X}/5\,{\rm keV})^{1/3}\ (10\,\rho_{\rm c}/r_{\rm L})^{1/3}$. Therefore, radio and non-thermal X-ray emission are produced by CCR of the secondary plasma ($\gamma_{\rm b} \approx 100$) and the incoherent curvature radiation of the primary beam ($\gamma_{\rm p} \gtrsim 10^5$), respectively. This is consistent with the one-dimensional (1D) particle distribution functions of the out-flowing relativistic plasma along the open magnetic field lines. Above a height of $0.5\, r_{\rm L}$ the sharp decrease of the curvature, $\kappa_{\rm c}$, shifts the photon energy to a lower band well below 1 keV. Moreover, the particle density number also drops due to the divergent magnetic field structure and the spherical expansion.

Non-dipolar components are excluded in the radio emission region and above it. The reason why non-thermal X-rays are mostly produced along the separatrix is two fold. First, the curvature radiation power scales as the curvature squared, $\kappa_{\rm c}^2$, and the particle charge squared, q^2, such that $\mathcal{P}_{\rm c} = (q^2/6\,\pi\,\varepsilon_0)\,\gamma^4\,c\,\kappa_{\rm c}^2$. Because the curvature, $\kappa_{\rm c}$, drastically decreases towards the centre of the polar cap, the associated curvature power also decreases, even faster than $\kappa_{\rm c}$. Furthermore, polar caps are known to show pair creation only in regions where the current density j satisfies $j > \rho\, c$ or $j/\rho\, c < 0$, where the physical boundaries depend on the obliquity (Timokhin & Arons 2013) and ρ is the corotating charge density. Also, magnetic field lines near the poles do not sustain pair cascades, producing only low energy primary particles. This leads to a hollow cone model reminiscent of the radio hollow cone model. Second, the particle density number, $n_{\rm e}$, along the separatrix is high due to the current required to support the transition layer between the open field-line region and the closed field-line region. Moreover, the current density decreases towards the centre for an inclined rotator and vanishes for an orthogonal rotator, as seen in Figs. 8 and 9 of Pétri (2022). Because the emissivity is proportional to the product, $n_{\rm e}\,\mathcal{P}_{\rm c}$, we expect the light curve to be formed essentially in the separatrix region, as postulated in our model. Adding some small resistivity to create a parallel accelerating electric field would only slightly change the value of the curvature, $\kappa_{\rm c}$. All the above results would be essentially unchanged for a resistive magnetosphere.

5. Conclusion

Based on the multi-wavelength light-curve fitting of PSR J2229+6114, we show that non-thermal X-ray photons emanate from a region located between the polar cap and the light cylinder, along the separatrix, at an altitude in the range of $r/r_{\rm L} \in [0.2, 0.55]$. The curvature radiation of the primary beam with Lorentz factor $\gamma_{\rm p} \gtrsim 10^5$ is responsible for this non-thermal X-ray emission, whereas the secondary plasma with $\gamma_{\rm b} \approx 100$ radiates radio photons. The extension of the X-ray region is controlled by the decrease in the open field line curvature along the separatrix, shifting the photon energy well below the X-ray band.

Acknowledgements. We are grateful to the referee and to P. Arumugasamy for helpful discussions and suggestions. This work has been supported by the CEFIPRA grant IFC/F5904-B/2018 and ANR-20-CE31-0010. SG acknowledges the support of the CNES. DM acknowledges the support of the Department of Atomic Energy, Government of India, under project No. 12-R&D-TFR-5.02-0700. The *Fermi*-LAT Collaboration acknowledges support for LAT development, operation and data analysis from NASA and DOE (United States), CEA/Irfu and IN2P3/CNRS (France), ASI and INFN (Italy), MEXT, KEK, and JAXA (Japan), and the K.A. Wallenberg Foundation, the Swedish Research Council and the National Space Board (Sweden). Science analysis support in the operations phase from INAF (Italy) and CNES (France) is also gratefully acknowledged. This work performed in part under DOE Contract DE-AC02-76SF00515. Work at NRL is supported by NASA.

References

Abdo, A. A., Ackermann, M., Ajello, M., et al. 2009, ApJ, 706, 1331
Abdo, A. A., Ajello, M., Allafort, A., et al. 2013, ApJS, 208, 17
Ajello, M., Atwood, W. B., Baldini, L., et al. 2022, Science, 376, 521
Arendt, P. N., Jr, & Eilek, J. A. 2002, ApJ, 581, 451
Arumugasamy, P., & Mitra, D. 2019, MNRAS, 489, 4589

Atwood, W. B., Abdo, A. A., Ackermann, M., et al. 2009, ApJ, 697, 1071
Bachetti, M., Markwardt, C. B., Grefenstette, B. W., et al. 2021, ApJ, 908, 184
Beskin, V. S., Gurevich, A. V., & Istomin, Y. N. 1993, Physics of the Pulsar Magnetosphere (Cambridge University Press)
Cerutti, B., Philippov, A. A., & Spitkovsky, A. 2016, MNRAS, 457, 2401
Coti Zelati, F., Torres, D. F., Li, J., & Viganò, D. 2020, MNRAS, 492, 1025
Gendreau, K. C., Arzoumanian, Z., & Okajima, T. 2012, SPIE Conf. Ser., 8443, 322
Gil, J., Gronkowski, P., & Rudnicki, W. 1984, A&A, 132, 312
Gil, J., Melikidze, G. I., & Geppert, U. 2003, A&A, 407, 315
Guillot, S., Kerr, M., Ray, P. S., et al. 2019, ApJ, 887, L27
Halpern, J. P., Camilo, F., Gotthelf, E. V., et al. 2001, ApJ, 552, L125
Harrison, F. A., Craig, W. W., Christensen, F. E., et al. 2013, ApJ, 770, 103
Íñiguez Pascual, D., Viganò, D., & Torres, D. F. 2022, MNRAS, 516, 2475
Johnston, S., Kramer, M., Karastergiou, A., et al. 2023, MNRAS, 520, 4801
Kalapotharakos, C., et al. 2019, ApJ, 883, L4
Kazbegi, A. Z., Machabeli, G. Z., & Melikidze, G. I. 1991, MNRAS, 253, 377
Kelner, S. R., Prosekin, A. Y., & Aharonian, F. A. 2015, AJ, 149, 33
Kuiper, L., & Hermsen, W. 2015, MNRAS, 449, 3827
Mitra, D. 2017, JApA, 38, 52
Philippov, A., Timokhin, A., & Spitkovsky, A. 2020, Phys. Rev. Lett., 124, 245101
Pétri, J. 2011, MNRAS, 412, 1870
Pétri, J. 2016, J. Plasma Phys., 82, 635820502
Pétri, J. 2022, A&A, 659, A147
Pétri, J. 2024, A&A, 687, A169
Pétri, J., & Mitra, D. 2020, MNRAS, 491, 80
Pétri, J., & Mitra, D. 2021, A&A, 654, A106
Radhakrishnan, V., & Cooke, D. J. 1969, Astrophys. Lett., 3, 225
Rothschild, R. E., Blanco, P. R., Gruber, D. E., et al. 1998, ApJ, 496, 538
Smith, D. A., Abdollahi, S., Ajello, M., et al. 2023, ApJ, 958, 191
Timokhin, A. N., & Arons, J. 2013, MNRAS, 429, 20
Timokhin, A. N., & Harding, A. K. 2019, ApJ, 871, 12
Usov, V. V. 2002, Proceedings of the 270 WE-Heraeus Seminar on Neutron Stars, Pulsars, and Supernova Remnants, MPE Report 278, eds. W. Becker, H. Lesch, & J. Trümper (Garching bei München: Max-Plank-Institut für extraterrestrische Physik), 240